


Spin-Photon Coupling for Atomic Qubit Devices in Silicon

Edyta N. Osika^{1,2,*} Sacha Kocsis^{1,2} Yu-Ling Hsueh^{1,2} Serajum Monir^{1,2} Cassandra Chua^{1,2} Hubert Lam^{3,‡} Benoit Voisin^{1,2} Michelle Y. Simmons^{2,3} Sven Rogge³ and Rajib Rahman^{1,2,†}

¹*School of Physics, University of New South Wales, Sydney, NSW 2052, Australia*

²*Silicon Quantum Computing Pty Ltd., Level 2, Newton Building, UNSW Sydney, Kensington, NSW 2052, Australia*

³*Centre for Quantum Computation and Communication Technology, School of Physics, University of New South Wales, Sydney, NSW 2052, Australia*

 (Received 6 May 2021; revised 6 March 2022; accepted 10 March 2022; published 4 May 2022)

Electrically addressing spin systems is predicted to be a key component in developing scalable semiconductor-based quantum-processing architectures, to enable fast spin-qubit manipulation and long-distance entanglement via microwave photons. However, single spins have no electric dipole, and therefore a spin-orbit mechanism must be integrated in the qubit design. Here, we propose to couple microwave photons to atomically precise donor spin-qubit devices in silicon using the hyperfine interaction intrinsic to donor systems and an electrically induced spin-orbit coupling. We characterize a one-electron system bound to a tunnel-coupled donor pair (1P-1P) using the tight-binding method, and then estimate the spin-photon coupling achievable under realistic assumptions. We address the recent experiments on double quantum dots (DQDs) in silicon and indicate the differences between DQD and 1P-1P systems. Our analysis shows that it is possible to achieve strong spin-photon coupling in 1P-1P systems in realistic device conditions without the need for an external magnetic field gradient.

DOI: [10.1103/PhysRevApplied.17.054007](https://doi.org/10.1103/PhysRevApplied.17.054007)

I. INTRODUCTION

Semiconductor spin qubits have now reached high enough figures of merit to envision error-corrected architectures for quantum-information processing [1–5]. Such architectures are expected to require both short-range spin-coupling mechanisms, achievable via, e.g., the exchange interaction [6–9], as well as chip-scale coupling mechanisms to allow for control electronics and quantum-information transfer [10]. Superconducting microwave cavities, which are used in the context of circuit quantum electrodynamics [11,12], are also suitable for coupling spin-based qubits at long distances [13] as the typical gigahertz microwave-cavity resonant frequencies can match the energy scales found in semiconductor-based spin devices [14].

Direct spin-photon coupling is challenging due to the small magnetic dipole interaction, usually on the order of 10 to 100 Hz [15], between an electron spin and the typical vacuum fluctuations of a resonant cavity. Instead, an electrical coupling between the two entities is preferable, which is also necessary for the development of electrically

driven spin resonance (EDSR) to increase qubit operation speed and scalability [7,16–24]. There are two requirements for creating electrical coupling: a charge dipole can be induced by localizing a spin across more than one quantum dot [25]; and spin-to-charge hybridization can be induced either through a natural spin-orbit mechanism (intrinsic SO, usually weak for electron systems), or by engineering a spin-orbit mechanism (extrinsic SO). An extrinsic SO mechanism can be created, for example, by using the transverse magnetic field gradient of a micromagnet [26–28]. Coupling spins to photons with an extrinsic SO mechanism has successfully been demonstrated in electrostatically defined quantum dots [29–34], yielding spin-photon coupling rates on the order of 10 MHz. These rates are sufficient to achieve the strong spin-photon coupling regime—a milestone where the spin-photon interaction rate exceeds both the qubit decoherence and cavity decay rates. While it has not been realized to date, achieving the strong coupling regime using an intrinsic SO mechanism would be desirable to ease device fabrication and scalability.

Electron spins bound to ³¹P donors in silicon form a relevant qubit platform for quantum-information processing with exceptionally long coherence times, demonstrated on the order of seconds [35,36], and the fastest two-qubit gate operations to date [9]. Recent progress on donor-bound spin qubits defined with the atomic precision of scanning

*e.osika@unsw.edu.au

†rajib.rahman@unsw.edu.au

‡Current address: Fachrichtung Physik, Universität des Saarlandes, 66123 Saarbrücken, Germany.

probe lithography [37,38] have included double and triple quantum-dot devices [9,39,40], where each quantum dot can be made of one or more dopants. Of note, phosphorus atoms host a nuclear spin [35,41], and the hyperfine interaction between the electron and the nuclear spins is the basis of a proposal for a hybrid spin qubit amenable to long-distance coupling via microwave photons [42]. An electrically induced spin-orbit interaction has also recently been observed in donor qubit devices [43], but its potential in electrically addressing spins remains to be explored.

Here, we describe a device architecture that combines both the ability to place dopant atoms with atomic precision in silicon and the use of their intrinsic SO mechanisms to couple spin qubits and microwave photons. The spin qubit itself consists of a single electron bound to two tunnel-coupled single ^{31}P donors, whose tunneling frequency is comparable to the resonant frequency of a nearby superconducting coplanar microwave resonator. Atomistic methods [44] are used to determine critical system parameters, i.e., the optimal donor separation and the corresponding tunnel coupling t_c and charge dipole moment d_c . We then investigate both the hyperfine (HF) [35,41,42] and the electrically induced spin-orbit (EISO) [43] mechanisms to realize the necessary spin-charge hybridization. An effective Hamiltonian approach is used to estimate the ratio, g_s/g_c , between the expected spin-photon and charge-photon couplings in a 1P-1P system. We use finite-element simulations of a cavity's electric field at the qubit position to estimate g_c , which we find to be comparable to what has recently been measured in gate-defined DQD systems [29,30]. Our results suggest that the strong spin-photon coupling regime is achievable for dopant systems in silicon under realistic qubit coherence and device electric field conditions.

II. THEORY

Previous theoretical analyses of qubit-cavity coupling in Si focused mostly on double quantum-dot systems, using an effective Hamiltonian framework and input-output theory [25,28,45]. In DQD devices, the spin-charge hybridization is achieved due to an inhomogeneous magnetic field that is usually created by a micromagnet deposited on the surface. The magnetic field gradient between the dots is included in the Hamiltonian as a term mixing electron spin and spatial degrees of freedom, which enables spin-photon coupling. Coupling the electron spin to the oscillating electric field has also been demonstrated in various DQD systems as mediated by intrinsic spin-orbit interaction or hyperfine interaction with the nuclear bath [46].

The nature of spin-charge hybridization is different in 1P-1P devices compared to DQD, since it arises from the hyperfine interaction between the electron and the small number of ^{31}P nuclear spins. Thanks to that it is possible to consider the electron-nuclear system as a whole and define

electron-nuclear spin-qubit states. Other works discussing spin-charge coupling in Si:P devices include the flip-flop qubit [42,47,48] and 1P-2P system [23,24]. Those proposals consider an asymmetry in the hyperfine interaction between the left and right dot, while our work investigates a symmetric (1P-1P) case, and demonstrates that this also produces viable spin-charge coupling. Our focus here is on a device design for optimized coupling to a superconducting resonator for long-distance two-qubit coupling, hence we discuss its feasibility in terms of all the relevant system parameters and cavity design.

Here, we formulate the effective 1P-1P Hamiltonian in the $|DI_L I_R S\rangle$ basis, where D defines an electron localized on the left or right donor ($|L\rangle$ or $|R\rangle$), I_L and I_R indicate the left and right nuclear spin (with a polarization $|\uparrow\rangle$ or $|\downarrow\rangle$) and S the electron spin ($|\uparrow\rangle$ or $|\downarrow\rangle$). We use the following 16×16 Hamiltonian in the described basis:

$$H = -t_c \tau_x + \epsilon \tau_z + h \gamma_e \mathbf{B} \cdot \mathbf{S} + \sum_{j=L,R} h \gamma_P \mathbf{B} \cdot \mathbf{I}_j + H_{\text{HF}}, \quad (1)$$

where h is Planck's constant, t_c is the tunneling rate between the two donors, ϵ is the relative detuning energy between the left and right donor states, $\mathbf{B} = (0, 0, B)$ is an external applied magnetic field, and $\gamma_e = 27.97$ GHz/T, $\gamma_P = -17.23$ MHz/T are the electron and nuclear spin gyromagnetic ratios, respectively. The Pauli matrices in the left and right donor basis are τ , while $\mathbf{S} = \frac{1}{2}\{\sigma_x^e, \sigma_y^e, \sigma_z^e\}$ and $\mathbf{I} = \frac{1}{2}\{\sigma_x^P, \sigma_y^P, \sigma_z^P\}$ are the electron and donor spin operators with σ^e (σ^P) being the Pauli matrices in the electron (donor) basis. H_{HF} is the Hamiltonian describing the HF interaction between electron and nuclear spins. It can be expressed as

$$H_{\text{HF}} = h A_L \mathbf{I}_L \cdot \mathbf{S} \otimes |L\rangle\langle L| + h A_R \mathbf{I}_R \cdot \mathbf{S} \otimes |R\rangle\langle R|, \quad (2)$$

where A_L (A_R) represents the hyperfine constant of the left (right) donor, assumed to be equal to the bulk value $A_L = A_R = 117$ MHz. The electron-nuclear spin product can be expressed as $\mathbf{I} \cdot \mathbf{S} = I_z S_z + \frac{1}{2}(I_+ S_- + I_- S_+)$.

Near zero detuning, the tunnel coupling t_c mixes the $|L\rangle$ and $|R\rangle$ states to create the bonding $|-\rangle$ and antibonding $|+\rangle$ states with $|\mp\rangle = (|L\rangle \pm |R\rangle)/\sqrt{2}$. We assume that the cavity field, with amplitude \mathcal{E}_0 and frequency f_r , has a nonzero polarization component along the x axis in Fig. 1, which is defined to be the 1P-1P axis. The operator $e\mathcal{E}_0 \mathbf{x}$ mixes the bonding $|-\rangle$ and antibonding $|+\rangle$ states, with a charge coupling rate g_c defined as $\hbar g_c \equiv \mathcal{E}_0 d_c = e\mathcal{E}_0 \langle -|x|+\rangle$. In the $\{|L\rangle, |R\rangle\}$ basis we can express the coupling Hamiltonian as

$$H_c = \hbar g_c (a + a^\dagger) \tau_x, \quad (3)$$

where a (a^\dagger) is the annihilation (creation) operator for the microwave resonator mode. This Hamiltonian H_c does

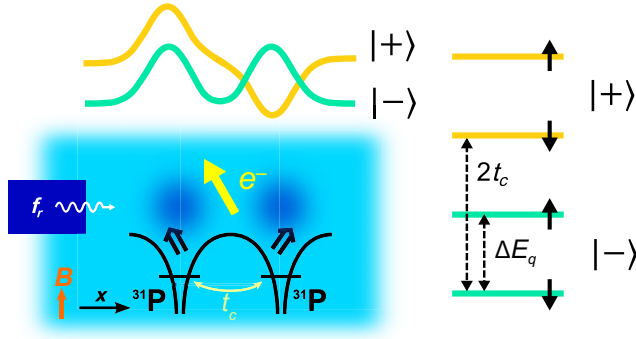


FIG. 1. Proposed device architecture. We consider a single electron (yellow arrow) confined between two phosphorus donors placed in the lattice of bulk silicon and separated in x direction. The two donor states are tunnel coupled (t_c) to form the bonding $|-\rangle$ and antibonding $|+\rangle$ orbital states. The qubit is formed between electron spin \downarrow and \uparrow states of the bonding orbital, with an energy splitting ΔE_q determined by the external magnetic field B and the hyperfine interaction between the electron and the nuclear spins of each P atoms (black arrows). The qubit electrically couples to the cavity at a resonant frequency f_r via a gate defined by STM lithography.

not directly mix spins since it is diagonal in nuclear and electron spin subspaces, i.e., $\langle D_1 I_i I_j S_a | H_c | D_2 I_k S_b \rangle = \delta_{il} \delta_{jk} \delta_{ab} \langle D_1 | H_c | D_2 \rangle$. However, as the hyperfine interaction is spatially dependent [see Eq. (2)] the H_{HF} induces hybridization of spin and orbital degrees of freedom in the system. We can expect this mixing to provide nonzero g_s values, i.e., H_c evaluated between eigenstates of opposite electron spin $\hbar g_s = |\langle \Psi_i | H_c | \Psi_j \rangle|$, and thus to enable the electrically driven spin rotations.

The dipole moment d_c and tunnel coupling t_c are two useful parameters to consider when discussing the spin-photon coupling g_s . The dipole d_c determines the rate of charge-photon coupling g_c , which sets an upper limit for g_s as the two coupling rates are proportional to each other. Tunneling is responsible for $|L\rangle$ and $|R\rangle$ state mixing, which is necessary for efficient electron movement between the dots or donors. This movement leads to periodic changes in the magnetic field for DQD or the hyperfine interaction for 1P-1P, which couples the spatial and spin degrees of freedom to enable electrically driven spin rotations. We look for a transition that involves electron $|\downarrow\rangle$ and $|\uparrow\rangle$ states of the bonding orbital, i.e., our qubit states (see Fig. 1). The cavity frequency should be matched to the energy splitting between those states—which is on the order of the electron Zeeman splitting $\gamma_e B$. As the proximity of the antibonding orbital to the qubit levels maximizes the degree of spin-charge hybridization, we aim also to set the tunneling rate $2t_c/h$ close to the qubit energy splitting. Considering the standard cavity frequency bandwidth range of 4–12 GHz, both DQD and 1P-1P systems

should be designed in a way that allows $\gamma_e B$ to be in that interval, and $2t_c/h$ to be close to that value.

We perform atomistic calculations using the NEMO3D package [49,50] to estimate the optimal donor separation in 1P-1P systems and its corresponding tunneling rate t_c and dipole moment d_c . In order to elucidate the challenges and feasibility of cavity coupling to donors, we also model DQD systems using the same method as above for comparison. For both systems we use a nearest-neighbor tight-binding Hamiltonian within the $sp^3 d^5 s^*$ band structure, where the positions of the P donors are defined with exact lattice site precision. The donors are represented by Coulomb potentials of a single positive charge—screened by the silicon dielectric constant $\epsilon_{\text{Si}} = 11.9$ and having a cutoff value of $U_0 = 3.782$ eV [44]. Quantum dots are represented by an external electrostatic potential of the form:

$$W(x, y, z) = \min_{i=1,2} [c_{xi}(x - x_i)^2 + c_{yi}(y - y_i)^2] + E_z z, \quad (4)$$

where c_{xi} and c_{yi} are the curvatures of the i th dot potential along x and y directions, respectively, and (x_i, y_i) is the i th dot center. E_z is the electric field applied from a top gate, which confines the electron close to the surface in the z direction. We use symmetric dots of potential curvatures $c_{xi} = c_{yi} = 1 \times 10^{-7}$ V/nm² and an electric field in z direction of $E_z = 10$ MV/m. This curvature corresponds to a dot radius of 35 nm, as calculated from the harmonic oscillator potential, $W(x) = \frac{1}{2} m \omega^2 x^2$, with the ground state proportional to $\exp(-x^2/r_0^2)$ and $r_0 = \sqrt{2\hbar/m\omega}$. At this curvature, the harmonic oscillator energy-level separation is equal to $\hbar\omega = 0.12367$ meV. As this energy is close to the tunnel coupling value of 40 μ eV, valley-orbital physics can alter the simple coupling picture between the cavity and the bonding and antibonding orbitals of quantum dots, as recently experimentally evidenced [51]. The situation is different for donors as tight-binding calculations yield an orbital splitting typically orders of magnitude larger than t_c —for 15–20 nm donor separation it is over 10 meV and falls to values comparable to the tunneling only for separation smaller than 7 nm. Therefore, we can neglect these higher orbital states in the rest of the paper, which focuses on donors only.

III. RESULTS

A. Tunneling and dipole moment

Using the atomistic model we calculate the tunneling energy and dipole moment for DQD [Figs. 2(a) and 2(b)] and 1P-1P [Figs. 2(c) and 2(d)] systems as a function of dot or donor separation Δx . The tunneling rate $2t_c/h$ represents the energy difference between the two lowest orbitals obtained with the tight-binding model, i.e., the bonding and antibonding orbitals. The range of Δx has been chosen to yield tunnel rates on the order of 10 GHz, to match

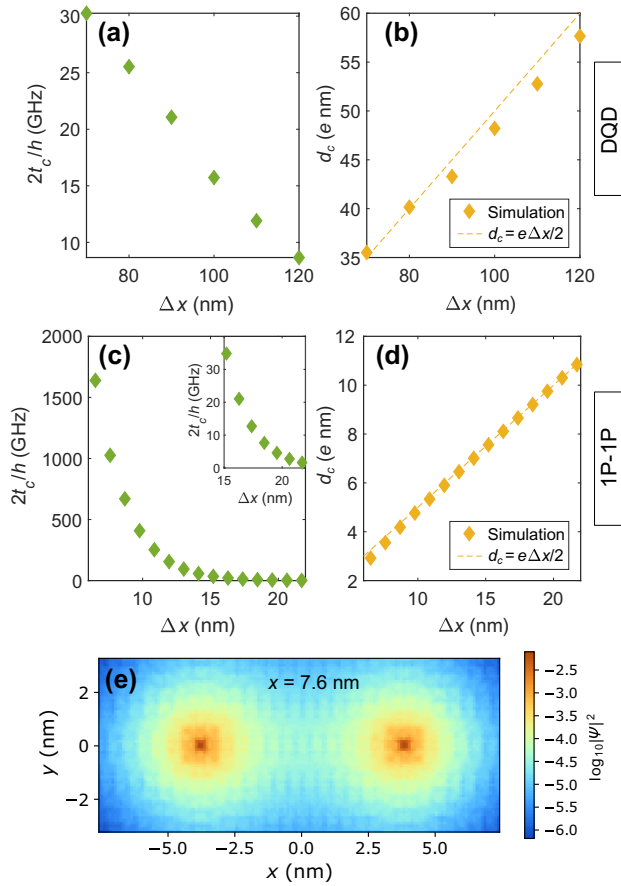


FIG. 2. Tunneling rate $2t_c$ (a),(c) and dipole moment d_c (b),(d) of a double quantum dot (a),(b) and two donor system (c),(d) as a function of dot or donor separation Δx . Dashed lines in (b),(d) show relation expected for the case of an ideal two-point dipole, i.e., $d_c = e\Delta x/2$. (e) Charge density of an electron localized within donors separated by 7.6 nm—for clarity plotted as a logarithm of $|\Psi|^2$. Plot shows the cross section of the device exactly at the donors' position in z direction.

the typical frequency range of coplanar microwave resonators. For the DQD system, the results correspond to recent experiments [29,30] in which $2t_c/h$ on the order of 10 GHz has been reported for dot separation of about 100 nm.

In the 1P-1P case, the electron wave function is significantly more localized than for quantum dots. The electron is strongly confined to donor regions [see Fig. 2(e) where $|\Psi|^2$ is plotted in logarithmic scale for better visibility] so the tunneling is considerably smaller than in quantum dots for the same Δx . For instance, the tunneling of approximately 30 GHz is obtained for dots separated by 70 nm, while the same tunneling for the 1P-1P system can be achieved only if bringing donors approximately 15 nm apart. The apparent qualitative difference between 1P-1P and DQD plots is due to the different Δx range to wave-function size ratio in both systems, as well as the specific choice of the dot potential profile. The large extent of the

electron wave function in quantum-dot devices results in limited variations of the corresponding tunnel coupling within the range of distances considered here, as shown in Fig. 2(a). In contrast, electron wave functions in donor devices are much more confined, with the tunnel coupling having a clear exponential behavior over just a 15-nm distance, dropping by 3 orders of magnitude as shown in Fig. 2(c). To operate in a $2t_c/h$ region comparable to cavity frequency bandwidth we should focus on donor separation of about 15–20 nm.

The calculated dipole moments shown in Figs. 2(b) and 2(d) follow approximately linear dependence as a function of the separation Δx , for both donors and DQDs. It can be noticed that the simulated values are in good agreement with the classical two-point dipole $d_c = e\Delta x/2$ [yellow dashed line in Figs. 2(b) and 2(d)], which we use in the following. For 1P-1P [Fig. 2(d)] in particular, due to the steep confining potential of the donors, the two-point dipole approximation is very accurate within the separation range we investigate. For smaller separations the orbital and valley energy splittings become comparable and we no longer have a well-defined two-level bonding-antibonding system, separated from other excited states. The slight deviation of the dipole for smallest Δx is a signature of this behavior.

The DQD simulations assume a parabolic shape of the dot potential and predict tunneling rates, which agree well with the experiment for this distance range [29,30]. More sophisticated electrical control, such as gate-tunable tunnel coupling, could be implemented in future work. Here, the first level of comparison between DQD and 1P-1P systems emphasizes the main challenge related to donors—the strong dependence of the tunnel rate with the interdonor distance. This dependence results in a stringent requirement to place the donors in a narrow Δx range of 15–20 nm for the tunnel coupling to be close to the cavity frequency. This limits the dipole moment, which can be achieved in 1P-1P systems to values approximately 5 times smaller than that of DQDs. However, this does not rule out the possibility of obtaining comparable charge-photon coupling g_c by maximizing the cavity field \mathcal{E}_0 at the donor sites. The strong localization of the electron wave function and the atomic precision of STM lithography allow the 1P-1P system to be placed in a high-field region of the cavity, as further explained in Sec. IV.

We also investigate the case of an electron bound to an asymmetric donor cluster system, namely the 1P-2P configuration. Because a 2P cluster presents a stronger localization potential to the electron compared to 1P, a detuning is required to bring the left and right donor levels on resonance in order to estimate a tunneling rate and dipole moment. This is done in the tight-binding model by adding a linear potential drop between the donors. We set the donors of the 2P cluster to be separated by two lattice constants, i.e., 1.08619 nm, along the y axis. Like

for the 1P-1P case, the dipole is still approximately proportional to $\Delta x/2$. Yet 1P-1P and 1P-2P systems present markedly different tunneling rates for the same cluster separation, e.g., $2t_c/h$ for 1P-2P (1P-1P) is equal to 38.5, 8.8, 0.4 GHz (252.7, 94.4, 12.7 GHz) for Δx equal to 10.86, 13.03, 17.38 nm, respectively. This considerable decrease of tunneling rate for 1P-2P with respect to 1P-1P can be intuitively understood as a result of a deeper overall donor potential and therefore stronger electron localization. This is undesirable for qubit-cavity coupling, since setting $2t_c$ resonant with a cavity would require bringing the 1P-2P cluster closer together, leading to a smaller dipole moment. However, that problem can be solved by loading the clusters with more electrons, e.g., three electrons for the 1P-2P system [24].

B. Hyperfine-mediated spin-photon coupling

We use the effective Hamiltonian defined in Eq. (1) to calculate the energy spectra of a 1P-1P system. We show in Fig. 3(a) the calculated energy levels of the system as a function of the detuning ϵ for two donors separated by $\Delta x = 18.47$ nm, in an applied external magnetic field $B = 0.2$ T. The tunneling rate for this separation, as shown in Fig. 2(c), is equal to $2t_c/h = 7.64$ GHz. Each of the four lines in Fig. 3(a) is itself a group of four distinct eigenstates, illustrated in Fig. 3(b). The left side of Fig. 3(b) shows the spectrum for a symmetric ($A_L = A_R$)

hyperfine interaction, and the right side for an asymmetric ($A_L > A_R$ or equivalently $\epsilon < 0$) interaction. The four eigenstates in each manifold differ only by nuclear spin configuration, and their order is determined by the HF interaction, as for $B = 0.2$ T it dominates over the nuclear Zeeman interaction.

For ease of notation, the eigenstates in Fig. 3(b) are only labeled by their dominant contributing state, and the labels do not show other basis states that have a finite weighting in the eigenstates. In fact, due to the off-diagonal terms in the hyperfine Hamiltonian H_{HF} , the states labeled in Fig. 3(b) are also composed of admixtures of other spin and orbital basis states. The nature of those admixtures can be predicted from the dominant contributing state and the form of H_{HF} , as HF causes electron-nuclear spin flip flops but does not change the total spin or the overall parity of the states. In contrast to the hyperfine interaction, the electric field of the resonator described by H_c interacts with the 1P-1P via the charge dipole matrix and thus changes the overall parity of the state.

We further estimate the spin-photon coupling $\hbar g_s$ by evaluating H_c between the H eigenstates at detuning $\epsilon = 0$. Nonzero matrix elements $\langle \psi_i | H_c | \psi_j \rangle$ indicate that the i th and j th states are coupled by a perturbation from the cavity electric field. That determines which transitions are possible, provided the cavity frequency f_r is resonant with the given level's energy splitting.

We can detail the composition of the ground state ψ_1 , and of the sixth eigenstate ψ_6 , to understand how the

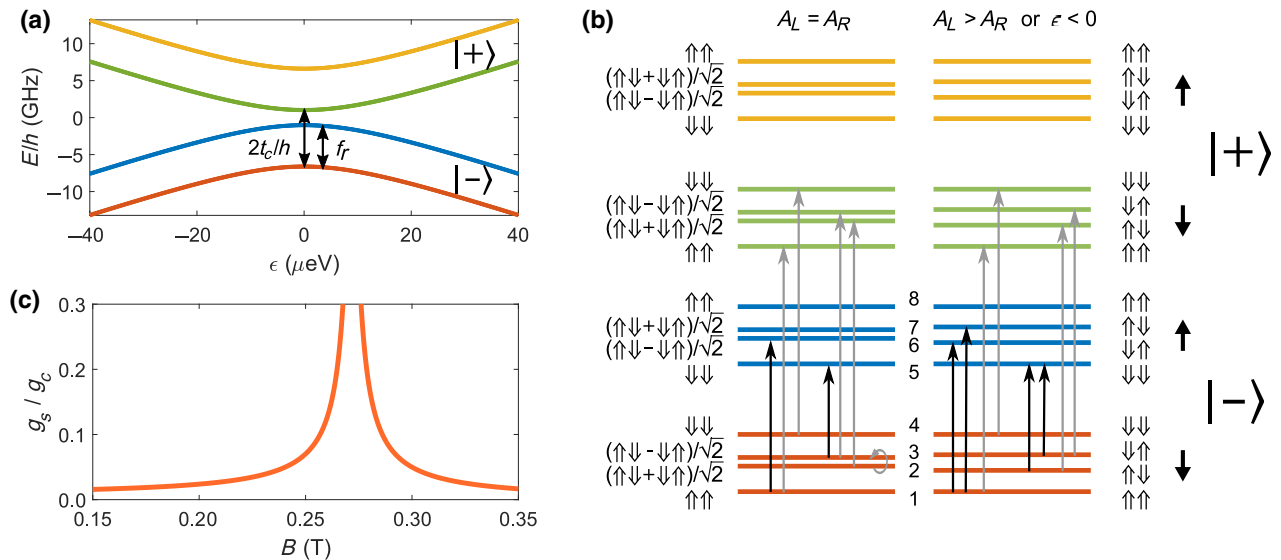


FIG. 3. (a) Energy spectra of the 1P-1P system as a function of detuning, as calculated within the effective Hamiltonian approach. Each line here is nearly fourfold degenerate due to different nuclear spin configurations. (b) Electron-nuclear energy levels for a symmetric ($A_L = A_R$) and asymmetric ($A_L > A_R$ or $\epsilon < 0$) hyperfine interaction. The color coding matches that of plot (a). Symbols $\{\uparrow, \downarrow\}$, $\{\uparrow, \downarrow\}$, $\{\uparrow, \downarrow\}$, $\{\uparrow, \downarrow\}$ describe the dominant contributing state of each eigenstate. Labels 1–8 enumerate the eigenstates. Black (gray) arrows indicate electron spin-flipping (conserving) transitions. (c) Spin-photon coupling g_s , expressed in g_c units as a function of the external magnetic field B for $2t_c/h = 7.64$ GHz.

admixture of different spin and orbital states can result in electrically available transitions:

$$\begin{aligned}
|\psi_1\rangle &= -0.7071(|L\rangle + |R\rangle)|\uparrow\uparrow\downarrow\rangle + 0.0035(|L\rangle + |R\rangle) \\
&\quad \times (|\uparrow\downarrow\rangle + |\downarrow\uparrow\rangle)|\uparrow\rangle - 0.0015(|L\rangle - |R\rangle) \\
&\quad \times (|\uparrow\downarrow\rangle - |\downarrow\uparrow\rangle)|\uparrow\rangle, \\
|\psi_6\rangle &= -0.4999(|L\rangle + |R\rangle)(|\uparrow\downarrow\rangle - |\downarrow\uparrow\rangle)|\uparrow\rangle \\
&\quad + 0.002(|L\rangle - |R\rangle)(|\uparrow\downarrow\rangle + |\downarrow\uparrow\rangle)|\uparrow\rangle \\
&\quad - 0.0146(|L\rangle - |R\rangle)|\uparrow\uparrow\downarrow\rangle, \tag{5}
\end{aligned}$$

In the above, nonzero transition elements driven by H_c appear between same-spin, opposite-orbital contributions from both eigenstates, i.e., between the first term of ψ_1 and the last term of ψ_6 etc. Note that this can be understood as the electric drive exciting the orbital basis from $|-\rangle$ to $|+\rangle$. Indeed, taking all the terms into account, we obtain a finite expected value $\hbar g_s^{1,6} = |\langle\psi_1|H_c|\psi_6\rangle| \approx 0.023\hbar g_c$. The same approach can be applied to identify all the other possible electron spin-flipping transitions, which are represented by the black arrows in Fig. 3(b). Note that these electrical transitions in tunnel-coupled donor systems can in principle also be used for EDSR, and parallel approaches have investigated the advantages of asymmetric clusters and multielectron systems in this context [23,24]. We ignore transitions to the antibonding electron spin-up states because of their significant energy separation with respect to the resonances considered in this paper. The transition matrix elements between states of the same spin but different spatial symmetry are equal to approximately $\hbar g_c$. As mentioned above, the transitions, which include an electron spin rotation always involve a nuclear spin transition as well—with the total spin of the joint electron-nuclear system being conserved. The configurations where the nuclear spins are polarized in the same direction, e.g., $\downarrow\downarrow\downarrow$, do not result in an available cavity-driven electron spin transition because there is no possible flip-flop transition, and the system is in the equivalent of a blockade regime.

A distinction must be made between the symmetric and asymmetric hyperfine cases. For the symmetric case, the configurations $\uparrow\downarrow$ and $\downarrow\uparrow$ form a nuclear spin singlet and triplet. This results in the state Ψ_1 (with dominant contribution of $\uparrow\uparrow$) to only couple to the nuclear singlet of opposite electron spatial symmetry and spin Ψ_6 [of dominant contribution of $\frac{1}{\sqrt{2}}(\uparrow\downarrow - \downarrow\uparrow)$], but not to the nuclear triplet Ψ_7 . In the case of an asymmetric hyperfine interaction between the left and the right donors, the nuclear singlet-triplet symmetry is broken as one of the configurations $\uparrow\downarrow$ or $\downarrow\uparrow$ is energetically favored, as depicted on the right-hand side of Fig. 3(b). Thus for the asymmetric hyperfine case there are four possible electrical transitions while for the symmetric case only two are allowed.

The splitting between $\uparrow\uparrow$ and $\downarrow\downarrow$ nuclear configuration, within the $|-\rangle$ or the $|+\rangle$ orbital, is a sum of hyperfine and nuclear Zeeman energies $(A_L + A_R)/4 \pm 2\gamma_P B$. As at the point of anticrossing the eigenstates contain some admixtures of different orbital and spin states, the actual energy splittings slightly deviate from the values mentioned above. This mixing also lifts the degeneracy of the nuclear spin singlet and triplet states. The resultant energy splitting is larger for smaller magnetic fields and for our parameters it is on the order of 0.1 MHz. In case of any asymmetry in the hyperfine interaction between the left and the right cluster, one of the configurations $\uparrow\downarrow$ or $\downarrow\uparrow$ is energetically favored and the nuclear-electron levels are further split by about $|A_L - A_R|/4$.

Since the antibonding $|+\rangle$ orbital plays a mediating role in the considered transition, the g_s coupling will depend on how strongly the orbitals are mixed and, consequently, on the relative values between $2t_c$ and the Zeeman splitting. We calculate g_s/g_c as a function of the magnetic field B while keeping t_c constant—see Fig. 3(c). We can see that the spin-photon coupling increases when the electron spin Zeeman splitting approaches $2t_c$ at about 0.272 T, that is the degeneracy point between the $|-\rangle\uparrow$ and $|+\rangle\downarrow$ states. Although g_s is highest there as it equals g_c , this point is also a hotspot where the spin qubit is most susceptible to charge decoherence—similarly to DQD systems.

C. Electrically induced spin-orbit interaction

Now we consider the effect of spin-orbit interaction on the donor system. As recently reported [43], a pronounced spin-orbit coupling arises in donor qubit devices in Si when placing P donors in a strong static electric field. It has been shown in the analysis of single-donor-electron spin-relaxation processes [43] that this effect, referred to here as EISO, can dominate over the Rashba and bulk silicon crystal SO interactions. In the following we focus only on the EISO effect. In a 1P-1P system, the EISO mechanism combined with an electric field difference between the two donor sites becomes equivalent to a magnetic field gradient used in DQDs to electrically induce spin-flip transitions. We include the following additional term H_{EISO} in the effective Hamiltonian H of Eq. (1):

$$H_{\text{EISO}}^e = \begin{pmatrix} E_y B_z + E_z B_y \\ E_z B_x + E_x B_z \\ E_x B_y + E_y B_x \end{pmatrix}^T \cdot \mathbf{C} \cdot \boldsymbol{\sigma} = E_y B_z C \sigma_x, \tag{6}$$

where E_x, E_y, E_z are the external electric field vector components and \mathbf{C} is a tensor representing the strength of the spin-orbit coupling, which arises from directional differences in single valleys as well as the valleys weights of the wave function localized within the P-donor potential. We can notice that only an electric field transverse to the applied magnetic field can produce nonzero elements in

the EISO Hamiltonian. For simplicity, we consider that the electric field is applied along the y axis, i.e., transverse to the z axis external magnetic field. Based on spin-relaxation anisotropy measurements, the C coefficient has been estimated to about $6 \times 10^{-14} e \text{ m/T}$ [43]. Because a difference in the SO strength is required between the left and right donor to obtain a finite spin-photon coupling, we assume different values of electric field E_y^L and E_y^R at the left and right donor sites. This spin-orbit Hamiltonian then reads

$$H_{\text{EISO}} = \begin{pmatrix} E_y^L B_z C & 0 \\ 0 & E_y^R B_z C \end{pmatrix} \otimes \sigma_x^e, \quad (7)$$

where the first matrix is in the $\{|L\rangle, |R\rangle\}$ basis. This SO mechanism has no influence on the nuclear spins, and the Hamiltonian is diagonal in the nuclear spin basis. Therefore, H_{EISO} enables electrically driven electron spin rotations whilst preserving nuclear polarization, e.g., $|\uparrow\uparrow\downarrow\rangle \rightarrow |\uparrow\uparrow\uparrow\rangle$, which is not possible via the HF interaction. Focusing on this particular transition, at a magnetic field $B_z = 0.2 \text{ T}$, we obtain $g_s/g_c \approx 1\%$ when the electric field difference between the dots is set to 12 MV/m ($E_y^L = 6 \text{ MV/m}$, $E_y^R = -6 \text{ MV/m}$), similar to those obtained with the HF mechanism. While the absolute values of these electric fields are reasonable for donor qubit devices, the opposite signs imply a steep field gradient that can be challenging to engineer in practice. This EISO coupling, however, presents an advantage over the HF mechanism in not requiring spin flip flops for electron spin rotations, and therefore enable spin-photon coupling regardless of the initial nuclear spin state.

In Fig. 4, g_s/g_c is shown for the possible transitions between pairs of eigenstates from Fig. 3(b). The calculations are done using $B_z = 0.2 \text{ T}$, $E_y^L = 15 \text{ MV/m}$, $E_y^R = -15 \text{ MV/m}$, with these electric field values chosen so that HF and EISO g_s would be of similar magnitude. For clarity, the resonances are plotted as a function of the frequency shifted by the electron Zeeman splitting $\Delta f = f_r - \gamma_e B$. The orange dashed lines represent the available transitions obtained when only the HF interaction is considered, while the black lines represent the transitions when both HF and EISO mechanisms are included. Both the zero and nonzero detuning cases are considered, and the numbers above each line indicate the eigenstates between which the transitions occur. The transitions labeled $1 \rightarrow 8$, $2 \rightarrow 7$, $3 \rightarrow 6$, and $4 \rightarrow 5$ are enabled by EISO only, while the small visible peaks of g_s/g_c on the order of 0.001 correspond to transitions for which both HF and EISO interaction are needed. These results clearly show that EISO offers additional means of coupling spins to microwave cavity, with the benefits of being insensitive to the nuclear polarization and relatively independent of HF-related g_s coupling.

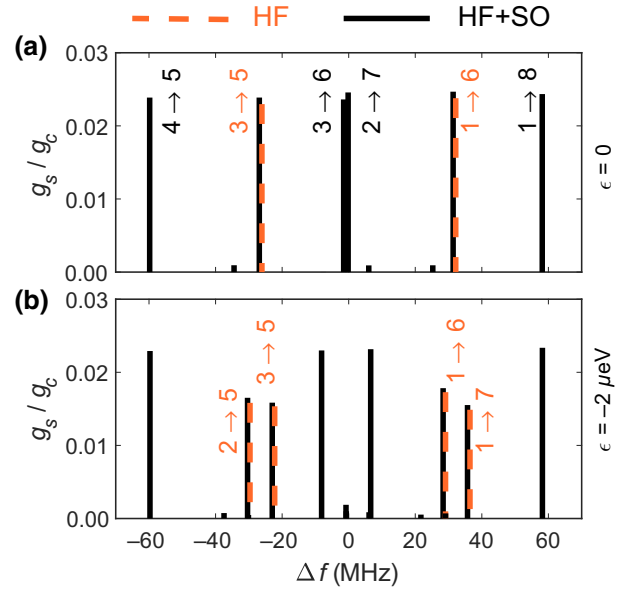


FIG. 4. Spin-photon coupling g_s expressed in g_c units for all possible transitions between the first two quadruplets (states 1–4 and 5–8). g_s is represented by a peak at each transition’s resonant frequency, with the x axis representing the frequency shifted by the electron Zeeman energy $\Delta f = f_r - \gamma_e B$. The black solid (orange dashed) line shows results for both the hyperfine and the spin-orbit (hyperfine only) interaction included in the Hamiltonian. Plots (a),(b) correspond to the cases of $\epsilon = 0$ and $\epsilon = -2 \mu\text{eV}$, respectively. These results are calculated for a magnetic field $B_z = 0.2 \text{ T}$ and external electric fields $E_y^L = 15 \text{ MV/m}$, $E_y^R = -15 \text{ MV/m}$.

D. Qubit operation and decoherence

The HF and EISO interactions enable different transitions in Fig. 4, at distinct resonant frequencies, and each of these frequencies can be treated as a possible working point for electron spin-qubit manipulation. The separation between HF- and EISO-enabled resonances is on the order of $(A_L + A_R)/8$, or tens of MHz, and it should be possible to distinguish the peaks originating from those two mechanisms with the frequency resolution offered by current cavity architectures.

Assuming all nuclear spin orientations have approximately the same probability (reasonable for temperatures on the order of 100 mK), the initial qubit state will appear in each of the four possible quadruplet eigenstates in the lowest branch of Fig. 3(b) equally often. Similarly to ESR experiments [52], at any given time we would observe only resonances corresponding to the current nuclear spin state. Additionally, as explained previously, not all initial qubit states are sensitive to electric field when solely the HF interaction is present in the system. Only including the EISO mechanism yields electrical transitions for any initial nuclear spin state. For example, the initial spin state $|\downarrow\downarrow\downarrow\rangle$ is insensitive to electric field for HF alone, but has

an allowed transition due to the EISO mechanism, see peak $4 \rightarrow 5$ in Fig. 4(a). The problem of nonresponsive initial states for the HF-only case could be overcome with nuclear spin polarization methods like NMR [53] or DNP [54,55]. Control over initial nuclear spin configuration, provided by these methods, would allow a single chosen resonance in Fig. 4 to be deterministically addressed.

Single-donor qubits can achieve very long coherence and relaxation times due to large excited-state energies and the absence of spurious nuclear spins in isotopically purified silicon [35,36]. The presence of a spin-orbit mechanism, necessary to enable electrical qubit manipulation, also exposes the qubit to charge noise, which can become the main source of decoherence [56], and make the strong spin-photon coupling regime challenging to achieve [19]. However, donor qubits can be embedded in a fully epitaxial structure while quantum dots are by definition pinned to an interface, usually rich in two-level fluctuators. Hence, noise figures as low as $0.094 \mu\text{eV}/\sqrt{\text{Hz}}$ (at 1 Hz) have been evidenced for a 2P-3P system [57], against a range of $0.3\text{--}2 \mu\text{eV}/\sqrt{\text{Hz}}$ for electrostatically defined quantum dots [58]. Spin decoherence rates in the 1–2 MHz range have been measured for DQDs [29,30], and the smaller dipole in donor systems at fixed tunneling frequencies implies that a smaller, or at least similar, spin decoherence rate for a 1P-1P strongly coupled to a microwave resonator could be expected, and this would allow reaching the strong coupling regime.

The 1P-1P system in principle does not require any electrostatic gates apart from the single lead controlling the detuning and providing contact for the resonator (this is discussed in more detail in Sec. IV). As spin-cavity coupling due to EISO requires large electric field gradients, the system utilizing the EISO mechanism would need additional leads to apply a local static E_y gradient. The polarization of the E field is along the y axis, perpendicular to the donor separation axis [see Eq. (7)], to allow both donors to remain at the same energy. While the presence of additional leads might affect the coherence properties of the system, we expect the large distance from the interface and the small dipole moment of a double-donor system to offer greater resilience to charge fluctuation noise compared to the subsurface DQDs confined with multiple gates [57].

Charge noise generates uncontrollable fluctuations in detuning, which shifts the qubit frequency and introduces phase decoherence. For the 1P-1P system we consider, detuning also causes asymmetry in the HF interaction, shifting the energies of some nuclear spin states. This noise-induced asymmetry thus results in additional electron spin-flipping transitions [see Fig. 3(b) with $1 \rightarrow 6$ transition available for symmetric and both $1 \rightarrow 6$ and $1 \rightarrow 7$ for the asymmetric case]. Figure 5 illustrates the frequency shift and strength of $1 \rightarrow 6$ and $1 \rightarrow 7$ transitions as a function of detuning. The height of the bars

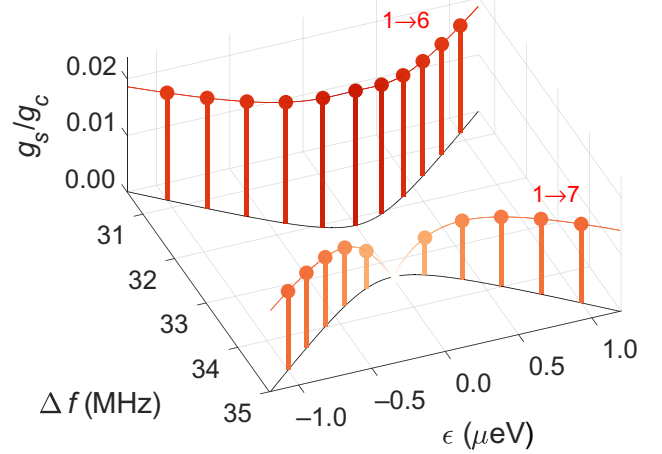


FIG. 5. The black lines show the relative frequency shift $\Delta f = f_r - \gamma_e B$ of the qubit ($1 \rightarrow 6$) and spurious ($1 \rightarrow 7$) transition as a function of detuning ϵ . The vertical bars show spin-photon coupling g_s/g_c of both $1 \rightarrow 6$ and $1 \rightarrow 7$ transitions for a given value of ϵ and Δf .

represents the g_s/g_c value for each resonance at a particular detuning. If we define $1 \rightarrow 6$ as the qubit rotation, the nearby $1 \rightarrow 7$ transition can be treated as a spurious one, outside of the qubit subspace. That electron spin transition represents another potential decoherence mechanism due to charge noise. Although g_s coupling of $1 \rightarrow 7$ transition can be strong far away from the anticrossing, it vanishes at zero detuning where the resonant frequencies of the qubit and spurious transitions are closest.

Finally, we comment on the prospect of realizing two-qubit gates with 1P-1P-based qubits. Long-distance qubit coupling via a superconducting cavity can be achieved either in the resonant or dispersive regime [59]. In particular, as described in Ref. [13] for the DQD case, i SWAP or CNOT operations can be realized in the dispersive regime by the exchange of virtual photons. The procedure for 1P-1P should be alike, however in contrast to the DQD, the donor-based system offers limited tunability of tunneling coupling after the device fabrication. In DQDs, the two-qubit gate is achieved by electrically tuning the tunnel coupling whilst remaining on the zero-detuning sweet spot. In a 1P-1P device, we expect to perform the two-qubit gate by controlling the detuning, as the qubit frequency can be dependent on ϵ (see $1 \rightarrow 6$ frequencies in Fig. 5). A more detailed analysis of this detuning dependence will be the subject of future work.

IV. RESONATOR SIMULATIONS

To enhance electric dipole coupling between a microwave resonator and a 1P-1P system, it is proposed to contact the ends of a resonator at the silicon surface to short phosphorous-doped leads at the qubit layer [60], 50 nm

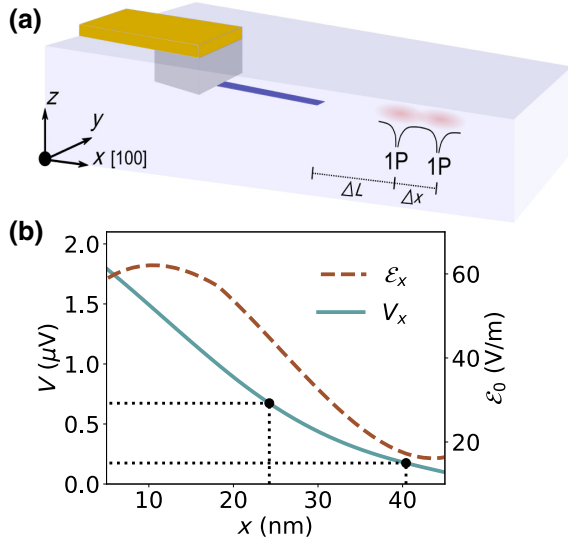


FIG. 6. (a) Illustration of one end of a $\lambda/2$ (Nb,Ti)N microwave resonator, terminating in a phosphorous δ -layer lead at the qubit plane, 50 nm below the silicon surface. The 1P-1P system is separated by approximately 15–20 nm, and placed $\Delta L > 20$ nm from the phosphorous δ -layer lead, using the nanometer precision of scanning-probe lithography. These two approximate distances are chosen to ensure that the 1P-1P tunneling frequency is in the 4–12 GHz range, and the tunneling frequency from the lead to the closest donor is far slower than any other time scale in the system. (b) Electric field and voltage from a single photon in the resonator mode, for a configuration similar to that illustrated in (a), simulated using Ansys HFSS. The voltage values are given at the two donor positions, and show a voltage detuning of approximately $\Delta V \sim 0.5 \mu\text{V}$.

beneath the surface, using vias as illustrated in Fig. 6(a). In this way, the resonator antinode can be brought to a distance slightly greater than 20 nm from one of the donors, to increase the differential lever arm.

A $\lambda/2$ superconducting microwave resonator in a notch configuration, similar in design to structures described in Ref. [61], is simulated using the Ansys HFSS package. The ends of the resonator are modeled to contact phosphorous δ -doped leads at the qubit layer, which have a sheet resistance of $R_{\text{xx}} = 350 \Omega/\square$ at 50 mK [60]. The simulated S_{21} parameter is fitted using the PYTHON package described in Ref. [62], and a loaded quality factor $Q_l \sim 5 \times 10^3$ is extracted from the fit, comparable to quality factors cited in Refs. [29,30]. Simulating an intracavity field at the single-photon level, the resulting electric field gradient in the silicon substrate is plotted along the 1P-1P axis in Fig. 6(b). Here, we take donor separation $\Delta x = 15\text{--}20$ nm as the correct order of magnitude ($\Delta x = 18.47$ nm has been used in spin-photon coupling simulations). We also assume a distance ΔL slightly more than 20 nm from the resonator's δ -layer termination to the nearest donor, to limit tunnel coupling between the donor and resonator lead. With these parameters and simulation of the electric

field from the cavity, a donor detuning of $\Delta V \sim 0.5 \mu\text{V}$ is estimated in Fig. 6(b). The engineered detuning of the 1P-1P from the high-impedance resonator can be compared to the detuning due to charge noise $\sigma_\epsilon = 0.17 \mu\text{eV}$ (1 s) measured for double donors in epitaxial silicon [57]. The fact that $e\Delta V/\sigma_\epsilon > 1$ suggests that dipole coupling to the resonator would be stronger than the effect of charge noise on the qubit.

In previous work [61], a potential difference of about $20 \mu\text{V}$ was inferred between the ends of their $\lambda/2$ resonator. A similar resonator design was used to demonstrate strong spin-photon coupling with electrostatically defined DQDs separated by about 100 nm [30]. It should be noted that the quantum well providing confinement along the z axis is about 50 nm beneath the silicon surface, and it can therefore be assumed that the DQDs are actually detuned by less than the maximum $20 \mu\text{V}$. It is also worthwhile to note that, in contrast to previous work [30,61], our Ansys HFSS simulations do not take into account the kinetic inductance of the thin superconducting film, which would further enhance the impedance of the cavity and therefore the resonant detuning at the qubit location.

The 1P-1P system described here will have a smaller electric dipole moment compared to DQDs, due to donor separation that is approximately one order of magnitude smaller for a similar tunneling rate. On the other hand, the resonator lead can be closer to donors than for DQDs, and the fact that the donors are in a region of higher field partly counterbalances the smaller electric dipole moment.

To reach the strong-coupling regime, the spin-photon coupling rate must be greater than both the cavity linewidth and the qubit decoherence rate. Simulations suggest that a charge-photon coupling rate $g_c = e\Delta V/2\hbar \sim 100$ MHz and $g_s/g_c = 0.02$ is realistic in the proposed device, to give a spin-photon coupling rate of 2 MHz. A resonator with fundamental frequency of 7.64 GHz should have a loaded quality factor close to 10^4 for a linewidth below 1 MHz, which is realistic with careful resonator design and fabrication.

V. CONCLUSIONS

We establish a modeling framework, which combines a tight-binding, effective Hamiltonian and finite-element high-frequency simulations, to estimate the spin-photon couplings that can realistically be achieved in donor systems in silicon. Of note, we use this framework to predict that strong spin-photon coupling is achievable in realistic donor device. We start from tight-binding wave-function simulations to estimate the tunnel couplings and associated charge dipole couplings as a function of the interdonor distance. Using an effective Hamiltonian approach that includes the hyperfine and EISO interactions for spin-orbit coupling, we show that electrically driven transitions exist between eigenstates. Our device proposal includes a $\lambda/2$

microwave resonator whose ends contact phosphorus δ -layer leads buried at the qubit layer, to allow the coupled donor system to be positioned in a region of high electric field gradient and thus enhance charge-photon coupling. Our simulations show that a spin-photon coupling rate of the order of 1 MHz, similar to what has been observed in DQD systems, are achievable in donor-based devices without an additional micromagnet fabricated close to the qubit. The simplified fabrication combined with excellent coherence properties are key advantages of using donors to build scalable and electrically addressable spin qubits.

ACKNOWLEDGMENTS

This research is conducted by the Australian Research Council Centre of Excellence for Quantum Computation and Communication Technology (CE170100012), the US Army Research Office under Contract No. W911NF-17-1-0202 and Silicon Quantum Computing Pty Ltd.

The research is undertaken with the assistance of resources and services from the National Computational Infrastructure (NCI) under an NCMAS 2020 allocation, supported by the Australian Government, and of the computational cluster Katana supported by Research Technology Services at UNSW Sydney.

-
- [1] A. G. Fowler, M. Mariantoni, J. M. Martinis, and A. N. Cleland, Surface codes: Towards practical large-scale quantum computation, *Phys. Rev. A* **86**, 032324 (2012).
- [2] C. D. Hill, E. Peretz, S. J. Hile, M. G. House, M. Fuechsle, S. Rogge, M. Y. Simmons, and L. C. L. Hollenberg, A surface code quantum computer in silicon, *Sci. Adv.* **1**, e1500707 (2015).
- [3] J. O’Gorman, N. H. Nickerson, P. Ross, J. J. L. Morton, and S. C. Benjamin, A silicon-based surface code quantum computer, *npj Quantum Inf.* **2**, 15019 (2016).
- [4] G. Pica, B. W. Lovett, R. N. Bhatt, T. Schenkel, and S. A. Lyon, Surface code architecture for donors and dots in silicon with imprecise and nonuniform qubit couplings, *Phys. Rev. B* **93**, 035306 (2016).
- [5] M. Veldhorst, H. G. J. Eenink, C. H. Yang, and A. S. Dzurak, Silicon CMOS architecture for a spin-based quantum computer, *Nat. Commun.* **8**, 1766 (2017).
- [6] M. Veldhorst, C. H. Yang, J. C. C. Hwang, W. Huang, J. P. Dehollain, J. T. Muhonen, S. Simmons, A. Laucht, F. E. Hudson, K. M. Itoh, A. Morello, and A. S. Dzurak, A two-qubit logic gate in silicon, *Nature* **526**, 410 (2015).
- [7] N. W. Hendrickx, D. P. Franke, A. Sammak, G. Scappucci, and M. Veldhorst, Fast two-qubit logic with holes in germanium, *Nature* **577**, 487 (2020).
- [8] T. F. Watson, S. G. J. Philips, E. Kawakami, D. R. Ward, P. Scarlino, M. Veldhorst, D. E. Savage, M. G. Lagally, M. Friesen, S. N. Coppersmith, M. A. Eriksson, and L. M. K. Vandersypen, A programmable two-qubit quantum processor in silicon, *Nature* **555**, 633 (2018).
- [9] Y. He, S. K. Gorman, D. Keith, L. Kranz, J. G. Keizer, and M. Y. Simmons, A two-qubit gate between phosphorus donor electrons in silicon, *Nature* **571**, 371 (2019).
- [10] L. M. K. Vandersypen, H. Bluhm, J. S. Clarke, A. S. Dzurak, R. Ishihara, A. Morello, D. J. Reilly, L. R. Schreiber, and M. Veldhorst, Interfacing spin qubits in quantum dots and donors—hot, dense, and coherent, *npj Quantum Inf.* **3**, 34 (2017).
- [11] J. Majer, J. M. Chow, J. M. Gambetta, J. Koch, B. R. Johnson, J. A. Schreier, L. Frunzio, D. I. Schuster, A. A. Houck, A. Wallraff, A. Blais, M. H. Devoret, S. M. Girvin, and R. J. Schoelkopf, Coupling superconducting qubits via a cavity bus, *Nature* **449**, 443 (2007).
- [12] M. A. Sillanpää, J. I. Park, and R. W. Simmonds, Coherent quantum state storage and transfer between two phase qubits via a resonant cavity, *Nature* **449**, 438 (2007).
- [13] M. Benito, J. R. Petta, and G. Burkard, Optimized cavity-mediated dispersive two-qubit gates between spin qubits, *Phys. Rev. B* **100**, 081412 (2019).
- [14] R. Hanson, L. P. Kouwenhoven, J. R. Petta, S. Tarucha, and L. M. K. Vandersypen, Spins in few-electron quantum dots, *Rev. Mod. Phys.* **79**, 1217 (2007).
- [15] R. J. Schoelkopf and S. M. Girvin, Wiring up quantum systems, *Nature* **451**, 664 (2008).
- [16] V. N. Golovach, M. Borhani, and D. Loss, Electric-dipole-induced spin resonance in quantum dots, *Phys. Rev. B* **74**, 165319 (2006).
- [17] M. Pioro-Ladrière, T. Obata, Y. Tokura, Y.-S. Shin, T. Kubo, K. Yoshida, T. Taniyama, and S. Tarucha, Electrically driven single-electron spin resonance in a slanting Zeeman field, *Nat. Phys.* **4**, 776 (2008).
- [18] S. Nadj-Perge, S. M. Frolov, E. P. A. M. Bakkers, and L. P. Kouwenhoven, Spin-orbit qubit in a semiconductor nanowire, *Nature* **468**, 1084 (2010).
- [19] K. D. Petersson, L. W. McFaul, M. D. Schroer, M. Jung, J. M. Taylor, A. A. Houck, and J. R. Petta, Circuit quantum electrodynamics with a spin qubit, *Nature* **490**, 380 (2012).
- [20] J. Salfi, J. A. Mol, D. Culcer, and S. Rogge, Charge-Insensitive Single-Atom Spin-Orbit Qubit in Silicon, *Phys. Rev. Lett.* **116**, 246801 (2016).
- [21] A. Corna, L. Bourdet, R. Maurand, A. Crippa, D. Kotekar-Patil, H. Bohuslavskyi, R. Laviéville, L. Hutin, S. Barraud, X. Jehl, M. Vinet, S. De Franceschi, Y.-M. Niquet, and M. Sanquer, Electrically driven electron spin resonance mediated by spin-valley-orbit coupling in a silicon quantum dot, *npj Quantum Inf.* **4**, 6 (2018).
- [22] H. Watzinger, J. Kukučka, L. Vukušić, F. Gao, T. Wang, F. Schäffler, J.-J. Zhang, and G. Katsaros, A germanium hole spin qubit, *Nat. Commun.* **9**, 3902 (2018).
- [23] Y. Wang, C.-Y. Chen, G. Klimeck, M. Y. Simmons, and R. Rahman, All-electrical control of donor-bound electron spin qubits in silicon, *ArXiv:1703.05370* (2017).
- [24] F. N. Krauth, S. K. Gorman, Y. He, M. T. Jones, P. Macha, S. Kocsis, C. Chua, B. Voisin, S. Rogge, R. Rahman, Y. Chung, and M. Y. Simmons, Flopping-Mode Electric Dipole Spin Resonance in Phosphorus Donor Qubits in Silicon, *Phys. Rev. Appl.* **17**, 054006 (2022).
- [25] G. Burkard, M. J. Gullans, X. Mi, and J. R. Petta, Superconductor–semiconductor hybrid-circuit quantum electrodynamics, *Nat. Rev. Phys.* **2**, 129 (2020).

- [26] G. Burkard and A. Imamoglu, Ultra-long-distance interaction between spin qubits, *Phys. Rev. B* **74**, 041307 (2006).
- [27] F. Beaudoin, D. Lachance-Quirion, W. A. Coish, and M. Pioro-Ladrière, Coupling a single electron spin to a microwave resonator: Controlling transverse and longitudinal couplings, *Nanotechnology* **27**, 464003 (2017).
- [28] X. Hu, Y.-X. Liu, and F. Nori, Strong coupling of a spin qubit to a superconducting stripline cavity, *Phys. Rev. B* **86**, 035314 (2012).
- [29] X. Mi, M. Benito, S. Putz, D. M. Zajac, J. M. Taylor, G. Burkard, and J. R. Petta, A coherent spin-photon interface in silicon, *Nature* **555**, 599 (2018).
- [30] N. Samkharadze, G. Zheng, N. Kalhor, D. Brousse, A. Sammak, U. C. Mendes, A. Blais, G. Scappucci, and L. M. K. Vandersypen, Strong spin-photon coupling in silicon, *Science* **359**, 1123 (2018).
- [31] F. Borjans, X. G. Croot, X. Mi, M. J. Gullans, and J. R. Petta, Resonant microwave-mediated interactions between distant electron spins, *Nature* **577**, 195 (2019).
- [32] A. J. Landig, J. V. Koski, P. Scarlino, U. C. Mendes, A. Blais, C. Reichl, W. Wegscheider, A. Wallraff, K. Ensslin, and T. Ihn, Coherent spin-photon coupling using a resonant exchange qubit, *Nature* **560**, 179 (2018).
- [33] A. J. Landig, J. V. Koski, P. Scarlino, C. Müller, J. C. Abadillo-Uriel, B. Kratochwil, C. Reichl, W. Wegscheider, S. N. Coppersmith, M. Friesen, A. Wallraff, T. Ihn, and K. Ensslin, Virtual-photon-mediated spin-qubit-transmon coupling, *Nat. Commun.* **10**, 5037 (2019).
- [34] J. V. Koski, A. J. Landig, M. Russ, J. C. Abadillo-Uriel, P. Scarlino, B. Kratochwil, C. Reichl, W. Wegscheider, G. Burkard, M. Friesen, S. N. Coppersmith, A. Wallraff, K. Ensslin, and T. Ihn, Strong photon coupling to the quadrupole moment of an electron in a solid-state qubit, *Nat. Phys.* **16**, 642 (2020).
- [35] J. T. Muhonen, J. P. Dehollain, A. Laucht, F. E. Hudson, R. Kalra, T. Sekiguchi, K. M. Itoh, D. N. Jamieson, J. C. McCallum, A. S. Dzurak, and A. Morello, Storing quantum information for 30 s in a nanoelectronic device, *Nat. Nanotechnol.* **9**, 986 (2014).
- [36] T. F. Watson, B. Weber, Y.-L. Hsueh, L. C. L. Hollenberg, R. Rahman, and M. Y. Simmons, Atomically engineered electron spin lifetimes of 30 s in silicon, *Sci. Adv.* **3**, e1602811 (2017).
- [37] M. Fuechsle, J. A. Miwa, S. Mahapatra, H. Ryu, S. Lee, O. Warschkow, L. C. L. Hollenberg, G. Klimeck, and M. Y. Simmons, A single-atom transistor, *Nat. Nanotechnol.* **7**, 242 (2012).
- [38] M. Koch, J. G. Keizer, P. Pakkiam, D. Keith, M. G. House, E. Peretz, and M. Y. Simmons, Spin read-out in atomic qubits in an all-epitaxial three-dimensional transistor, *Nature* **571**, 371 (2019).
- [39] T. F. Watson, B. Weber, J. A. Miwa, S. Mahapatra, R. M. P. Heijnen, and M. Y. Simmons, Transport in asymmetrically coupled donor-based silicon triple quantum dots, *Nano Lett.* **14**, 1830 (2014).
- [40] P. Pakkiam, A. V. Timofeev, M. G. House, M. R. Hogg, T. Kobayashi, M. Koch, S. Rogge, and M. Y. Simmons, Single-Shot Single-Gate rf Spin Readout in Silicon, *Phys. Rev. X* **8**, 041032 (2018).
- [41] S. J. Hile, L. Fricke, M. G. House, E. Peretz, C. Y. Chen, Y. Wang, M. Broome, S. K. Gorman, J. G. Keizer, R. Rahman, and M. Y. Simmons, Addressable electron spin resonance using donors and donor molecules in silicon, *Sci. Adv.* **4**, eaaq1459 (2018).
- [42] G. Tosi, F. A. Mohiyaddin, V. Schmitt, S. Tenberg, R. Rahman, G. Klimeck, and A. Morello, Silicon quantum processor with robust long-distance qubit couplings, *Nat. Commun.* **8**, 450 (2017).
- [43] B. Weber, Y.-L. Hsueh, T. F. Watson, R. Li, A. R. Hamilton, L. C. L. Hollenberg, R. Rahman, and M. Y. Simmons, Spin-orbit coupling in silicon for electrons bound to donors, *npj Quantum Inf.* **4**, 61 (2018).
- [44] S. Ahmed*, N. Kharche*, R. Rahman*, M. Usman*, S. Lee*, H. Ryu, H. Bae, S. Clark, B. Haley, M. Naumov, F. Saied, M. Korkusinski, R. Kennel, M. McLennan, T. B. Boykin, and G. Klimeck, in *Encyclopedia of Complexity and Systems Science*, edited by R. A. Meyers (Springer New York, New York, NY, 2009), p. 5745.
- [45] M. Benito, X. Mi, J. M. Taylor, J. R. Petta, and G. Burkard, Input-output theory for spin-photon coupling in Si double quantum dots, *Phys. Rev. B* **96**, 235434 (2017).
- [46] E. A. Laird, C. Barthel, E. I. Rashba, C. M. Marcus, M. P. Hanson, and A. C. Gossard, Hyperfine-Mediated Gate-Driven Electron Spin Resonance, *Phys. Rev. Lett.* **99**, 246601 (2007).
- [47] P. Boross, G. Széchenyi, and A. Pályi, Hyperfine-assisted fast electric control of dopant nuclear spins in semiconductors, *Phys. Rev. B* **97**, 245417 (2018).
- [48] B. Hetényi, P. Boross, and A. Pályi, Hyperfine-assisted decoherence of a phosphorus nuclear-spin qubit in silicon, *Phys. Rev. B* **100**, 115435 (2019).
- [49] G. Klimeck, F. Oyafuso, T. B. Boykin, R. C. Bowen, and P. von Allmen, Development of a nanoelectronic 3-D (NEMO 3-D) simulator for multimillion atom simulations and its application to alloyed quantum dots, *Comput. Model. Eng. Sci.* **3**, 601 (2002).
- [50] G. Klimeck, S. S. Ahmed, H. Bae, N. Kharche, S. Clark, B. Haley, S. Lee, M. Naumov, H. Ryu, F. Saied, M. Prada, M. Korkusinski, T. B. Boykin, and R. Rahman, Atomistic simulation of realistically sized nanodevices using nemo 3-D—part I: Models and benchmarks, *IEEE Trans. Electron. Devices* **54**, 2079 (2007).
- [51] X. Mi, S. Kohler, and J. R. Petta, Landau-Zener interferometry of valley-orbit states in Si/SiGe double quantum dots, *Phys. Rev. B* **98**, 161404 (2018).
- [52] Y. Wang, C.-Y. Chen, G. Klimeck, M. Y. Simmons, and R. Rahman, Characterizing Si:P quantum dot qubits with spin resonance techniques, *Sci. Rep.* **6**, 31830 (2016).
- [53] J. J. Pla, K. Y. Tan, J. P. Dehollain, W. H. Lim, J. J. L. Morton, F. A. Zwanenburg, D. N. Jamieson, A. S. Dzurak, and A. Morello, High-fidelity readout and control of a nuclear spin qubit in silicon, *Nature* **496**, 334 (2013).
- [54] A. Abragam and M. Goldman, Principles of dynamic nuclear polarisation, *Rep. Progr. Phys.* **41**, 395 (1978).
- [55] S. Simmons, R. M. Brown, H. Riemann, N. V. Abrosimov, P. Becker, H.-J. Pohl, M. L. W. Thewalt, K. M. Itoh, and J. J. L. Morton, Entanglement in a solid-state spin ensemble, *Nature* **470**, 69 (2011).
- [56] J. Yoneda, K. Takeda, T. Otsuka, T. Nakajima, M. R. Delbecq, G. Allison, T. Honda, T. Kodera, S. Oda, Y. Hoshi, N. Usami, K. M. Itoh, and S. Tarucha, A quantum-dot

- spin qubit with coherence limited by charge noise and fidelity higher than 99.9%, *Nat. Nanotechnol.* **13**, 102 (2018).
- [57] L. Kranz, S. K. Gorman, B. Thorgrimsson, Y. He, D. Keith, J. G. Keizer, and M. Y. Simmons, Exploiting a single-crystal environment to minimize the charge noise on qubits in silicon, *Adv. Mater.* **32**, 2003361 (2020).
- [58] T. Struck, A. Hollmann, F. Schauer, O. Fedorets, A. Schmidbauer, K. Sawano, H. Riemann, N. V. Abrosimov, Ł. Cywiński, D. Bougeard, and L. R. Schreiber, Low-frequency spin qubit energy splitting noise in highly purified $^{28}\text{Si}/\text{SiGe}$, *npj Quantum Inf.* **6**, 40 (2020).
- [59] D. J. van Woerkom, P. Scarlino, J. H. Ungerer, C. Müller, J. V. Koski, A. J. Landig, C. Reichl, W. Wegscheider, T. Ihn, K. Ensslin, and A. Wallraff, Microwave Photon-Mediated Interactions Between Semiconductor Qubits, *Phys. Rev. X* **8**, 041018 (2018).
- [60] F. J. Ruess, L. Oberbeck, M. Y. Simmons, K. E. J. Goh, A. R. Hamilton, T. Hallam, S. R. Schofield, N. J. Curson, and R. G. Clark, Toward atomic-scale device fabrication in silicon using scanning probe microscopy, *Nano Lett.* **4**, 1969 (2004).
- [61] N. Samkharadze, A. Bruno, P. Scarlino, G. Zheng, D. P. DiVincenzo, L. DiCarlo, and L. M. K. Vandersypen, High-Kinetic-Inductance Superconducting Nanowire Resonators for Circuit QED in a Magnetic Field, *Phys. Rev. Appl.* **5**, 044004 (2016).
- [62] S. Probst, F. B. Song, P. A. Bushev, A. V. Ustinov, and M. Weides, Efficient and robust analysis of complex scattering data under noise in microwave resonators, *Rev. Sci. Instrum.* **86**, 024706 (2015).